

HYDRODYNAMIC AND NUMERICAL MODELING OF A SPHERICAL HOMOGENEOUS DYNAMO EXPERIMENT

*C.B. Forest, R.A. Bayliss, R.D. Kendrick, M.D. Nornberg,
R. O'Connell, E.J. Spence*

Department of Physics, University of Wisconsin, Madison, Wisconsin 53711, USA

A spherical, homogeneous kinematic dynamo is investigated both experimentally and theoretically at the University of Wisconsin. Previous kinematic dynamo studies are extended by optimizations in flow geometries which lower the critical magnetic Reynolds number for self-excitation. The stretch-twist-fold dynamo model is used to describe the physical mechanism for magnetic field generation in a simple two-vortex flow. The possibility of producing such flows in liquid sodium is studied in a water experiment. Mechanically driven flows generated by rotating impellers enclosed in a spherical vessel are characterized by measurements of the velocity field using Laser Doppler Velocimetry. The mean flows studied are predicted to lead to self-excitation of magnetic eigenmodes. The sodium dynamo experiment is described.

Introduction. The question of how magnetic fields are generated by flows in conducting fluids is referred to as the "dynamo" problem. Theoretical research into dynamo mechanisms has been actively pursued for several decades. Until quite recently, however, probing of the dynamo problem has been limited to analytic calculations, numerical models, and observational studies; experiments, the critical tests of dynamo theory, have been scarce.

Two important questions to be addressed by dynamo theories and experiments are: (1) what class of flow geometries and velocity fields (presumably turbulent) lead to self-excitation of magnetic fields? (2) how does a self-generated magnetic field affect the velocity field and bring about saturation of an otherwise growing magnetic field?

In answering the first question, one looks for solutions to the magnetic induction equation in which the magnetic field is growing. The magnetic induction equation is derived from Faraday's law and the equation describing the generation of current by motion of a conductor across a magnetic field. It is given by

$$\frac{\partial \mathbf{B}}{\partial t} = \nabla \times (\mathbf{V} \times \mathbf{B}) + \frac{1}{\sigma \mu_0} \nabla^2 \mathbf{B}, \quad (1)$$

where \mathbf{B} is the magnetic field, \mathbf{V} is the velocity field, and σ is the conductivity of the fluid. The validity of the induction equation is not in doubt; it has been tested repeatedly in the context of plasma physics. The untested part of the kinematic dynamo problem concerns the geometry of the flow. Dynamos require a flow geometry in which the current generated by the fluid flow across a seed magnetic field produces a new magnetic field that amplifies and reinforces the original seed field. The goal is to determine the boundary conditions and flow topologies which produce dynamos. We restrict our search to flows in a simply connected container, unconstrained by baffles, in which the medium is electrically homogeneous [1].

The second question is a study of the non-linear coupling of the induction equation (1) to the equation of motion governing the fluid velocity:

$$\rho \left(\frac{\partial \mathbf{V}}{\partial t} + \mathbf{V} \cdot \nabla \mathbf{V} \right) = \mathbf{J} \times \mathbf{B} + \rho \nu \nabla^2 \mathbf{V} - \nabla p, \quad (2)$$

where ν is the viscosity and p is the pressure. As a self-generated magnetic field grows, the relative strength of the Lorentz force increases, changes the velocity field, and ultimately alters the growth rate of the magnetic field. Energy conservation defines a saturation limit where the applied mechanical energy is balanced by dissipation, though a number of other saturation mechanisms may occur. For instance, the mechanical driving force may balance the Lorentz force, the Lorentz force may distort the mean velocity field, or turbulence in the velocity field may cause a small scale back reaction.

There is evidence of some experimental progress in identifying flow geometries which lead to dynamo action. Notably, Lowes and Wilkinson constructed an electrically homogeneous kinematic dynamo (based on a theorem by Herzenberg) by embedding two rotating, conducting spheres in a larger conducting block [2, 3, 4]. The successful dynamo experiments in Karlsruhe and Riga show that new flow topologies are made possible by using liquid metal rather than solid conductors. Both of these experiments demonstrate kinematic dynamo action using helical flows of liquid sodium which cannot be realized by rotating solid conductors [5, 6]. Pipes and helical baffles constrain these flows by separating the sodium into a number of different regions, so although these experiments could be considered electrically homogeneous, they are not mechanically homogeneous and do not address the large scale back-reaction of the self-generated magnetic field on the flow. No experiments yet demonstrate dynamo action in which the velocity field is unconstrained by pipes and baffles on the scale the magnetic field is generated.

The goal of the Madison Dynamo Experiment is to construct an *electrically* and *mechanically* homogeneous dynamo in which the geometry is simply connected, the fluid is surrounded by a vacuum region, and for which the flow is driven but free to respond to Lorentz forces induced by the generated magnetic fields [1]¹. The Madison Dynamo Experiment consists of a 1 m diameter, stationary spherical vessel filled with liquid sodium with 150 kW of mechanical energy input from impellers. The spherical geometry is motivated in part by theoretical kinematic dynamo studies which show that simple axisymmetric flows can generate self-excited magnetic eigenmodes [9, 10, 11, 12]. An example is shown in Fig. 1. Like the experiments at Karlsruhe and Riga, this flow has strong helicity but is generated without the constraints of pipes. Previous studies indicate that for the proper flow geometry, a magnetic eigenmode can grow provided the magnetic Reynolds number

$$Rm = \mu_0 a \sigma V_0 \quad (3)$$

exceeds a critical value Rm_c . Here a is a scale length taken to be the radius for spherical geometry, σ is the fluid conductivity (10^7 mho/m for liquid sodium), and V_0 is the peak speed of the mean flow. The required value of Rm_c depends upon the details of the velocity field. Target velocity fields with low values of Rm_c are more easily achieved in an experiment since the required inventory of liquid sodium and required fluid speed are smaller.

¹Similar experiments are being performed at the CNRS, Caderache [7] and at the University of Maryland [8].

Fig. 1.
ric flow
consistin
tices. T
tal.

The
Experim
of ω^2 -d
excite f
provide
profiles
possibil
hydrod
which a
describ
1.
Numeri
equatio

where
bounda
termin
phenom
great d
spheric

1.
the kin
unstab
magnet
of varia

where
resistiv
discret

each cl
primar
 $\mathbf{B}_i(\mathbf{x})$.

induction

(2)

netic field
e velocity
y conser-
balanced
ccur. For
e Lorentz
field may

w geome-
nstructed
Herzen-
ng block
now that
olid con-
on using
conduc-
e sodium
e consid-
d do not
d on the
city field
nerated.

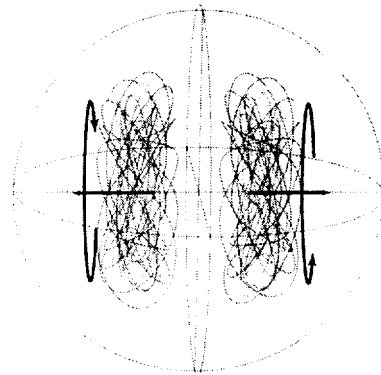
ctrically
ply con-
e flow is
magnetic
station-
l energy
eoretical
an gen-
own in
g helic-
indicate
ded the

(3)

rdius for
(m), and
s upon
Rm_c are
sodium

niversity

Fig. 1. Streamlines for an axisymmetric flow proposed by Dudley and James, consisting of two counter flowing vortices. The axis of symmetry is horizontal.



This paper documents progress towards constructing the Madison Dynamo Experiment. The first section presents results of a numerical optimization study of ω^2 -dynamo systems which has identified velocity fields in a sphere which self-excite for values of Rm_c considerably lower than previously reported. These results provide target flows for experiments. The dynamo produced by one of the flow profiles is described in terms of the stretch-twist-fold process in Section 1.3. The possibility of generating the target flows is addressed in Section 2 which describes hydrodynamic experiments that demonstrate that velocity fields can be produced which are predicted to be kinematic dynamos with low values of Rm_c . Section 3 describes the sodium dynamo experiment.

1. Optimizing axisymmetric flows for spherical kinematic dynamos.

Numerical techniques are generally required for solving the magnetic induction equation,

$$\frac{\partial \mathbf{B}}{\partial t} = \nabla \times (\mathbf{V} \times \mathbf{B}) + \frac{1}{Rm} \nabla^2 \mathbf{B}, \quad (4)$$

where the equation is now in dimensionless form. Once the velocity field and boundary conditions are specified, the evolution of the magnetic field can be determined. We choose to work in a spherical geometry since it applies to natural phenomena, it leads naturally to a classification of possible flow topologies, and a great deal of work has already been done in searching for dynamo solutions in spherical systems [9, 10, 11, 13].

1.1. Numerical formulation of the kinematic dynamo in a sphere. In solving the kinematic dynamo problem, one searches for velocity fields which are linearly unstable to magnetic perturbations and thereby generate exponentially growing magnetic fields $\mathbf{B} \propto e^{\lambda t}$. Assuming this exponential time dependence, separation of variables in (4) leads to a linear eigenvalue equation for λ :

$$\lambda \mathbf{B} = Rm \nabla \times (\mathbf{V} \times \mathbf{B}) + \nabla^2 \mathbf{B}, \quad (5)$$

where the equation is recast in terms of normalized variables and the characteristic resistive diffusion time $\tau_\sigma = \mu_0 \sigma a^2$. The solution to (5) consists of a series of discrete eigenmodes

$$\mathbf{B} = \sum_i \mathbf{B}_i(\mathbf{x}) \exp(\lambda_i t), \quad (6)$$

each characterized by complex frequencies λ_i . The kinematic dynamo problem is primarily concerned with finding the least damped, or fastest growing, eigenmode $\mathbf{B}_i(\mathbf{x})$. If $\Re(\lambda_i) > 0$ the system is a dynamo.

Exploiting the divergence-free nature of both the magnetic field and velocity field (assuming the fluid is incompressible), a vector potential is defined for both the velocity and the magnetic field in terms of spherical harmonic functions such that [13]:

$$\mathbf{V} = \sum_{l,m} \nabla \times t_\ell^m(r) Y_\ell^m(\theta, \phi) \hat{r} + \sum_{l,m} \nabla \times \nabla \times s_\ell^m(r) Y_\ell^m(\theta, \phi) \hat{r}, \quad (7)$$

$$\mathbf{B} = \sum_{l,m} \nabla \times T_\ell^m(r) Y_\ell^m(\theta, \phi) \hat{r} + \sum_{l,m} \nabla \times \nabla \times S_\ell^m(r) Y_\ell^m(\theta, \phi) \hat{r}. \quad (8)$$

The fields separate naturally into two components. The first series in each field are labeled as *toroidal* components of the field. They can be identified with field lines constrained to spherical surfaces of constant r , *i.e.* they are vector fields with no radial component. They are specified by the scalar profile functions $t_\ell^m(r)$ and $T_\ell^m(r)$. The second series are labeled as *poloidal* and are specified by the scalar functions profile functions $s_\ell^m(r)$ and $S_\ell^m(r)$. These fields have a radial component. In fact, the scalar functions themselves can be identified with the spherical harmonic representation of the radial part of the vector field. For example, the magnetic field is

$$B_r(r, \theta, \phi) = \sum_{l,m} \frac{\ell(\ell+1)}{r^2} S_\ell^m(r) Y_\ell^m(\theta, \phi), \quad (9)$$

$$B_\theta(r, \theta, \phi) = \sum_{l,m} \frac{1}{r} \frac{dS_\ell^m}{dr} \frac{\partial Y_\ell^m}{\partial \theta} + \frac{T_\ell^m}{r \sin \theta} \frac{\partial Y_\ell^m}{\partial \phi}, \quad (10)$$

$$B_\phi(r, \theta, \phi) = \sum_{l,m} \frac{1}{r \sin \theta} \frac{dS_\ell^m}{dr} \frac{\partial Y_\ell^m}{\partial \phi} - \frac{T_\ell^m}{r} \frac{\partial Y_\ell^m}{\partial \theta}. \quad (11)$$

The absence of flow through the surface of the sphere, an assumed no-slip condition, and non-singularity at the origin imply

$$\begin{aligned} s_\ell^m &= \frac{ds_\ell^m}{dr} = t_\ell^m = 0 \quad \text{at } r = a, \quad \text{and} \\ s_\ell^m &= t_\ell^m = 0 \quad \text{at } r = 0. \end{aligned}$$

On the surface of the sphere the magnetic field in the vessel must match a vacuum solution of the magnetic field outside the sphere which requires

$$\begin{aligned} T_\ell^m &= \frac{dT_\ell^m}{dr} + \frac{\ell S_\ell^m}{r} = 0 \quad \text{at } r = a, \quad \text{and} \\ T_\ell^m &= S_\ell^m = 0 \quad \text{at } r = 0. \end{aligned}$$

A natural consequence is that only poloidal magnetic fields will be observable outside the sphere since the toroidal magnetic field is entirely contained within the sphere.

The problem reduces to solving a coupled set of differential equations for the radial profile functions $T_\ell^m(r)$ and $S_\ell^m(r)$ given the profile functions $t_\ell^m(r)$ and $s_\ell^m(r)$. This set is derived by substituting the spherical harmonic expansions into (5). The orthogonality of the toroidal and poloidal fields allows the equation to be split into two sets of coupled equations. Each equation describes the evolution of a single magnetic mode in terms of the interaction of magnetic modes with velocity modes:

$$\begin{aligned} \frac{\partial^2 S_\gamma}{\partial r^2} - \lambda S_\gamma - \frac{\ell_\gamma(\ell_\gamma + 1)}{r^2} S_\gamma &= \frac{\text{Rm}}{r^2} \sum_{\alpha, \beta} t_\alpha S_\beta \rightarrow S_\gamma + \\ &+ t_\alpha T_\beta \rightarrow S_\gamma + s_\alpha T_\beta \rightarrow S_\gamma + s_\alpha S_\beta \rightarrow S_\gamma, \quad (12) \end{aligned}$$

$$\frac{\partial^2 T_\gamma}{\partial r^2} - \lambda T_\gamma - \frac{\ell_\gamma(\ell_\gamma + 1)}{r^2} T_\gamma = \frac{\text{Rm}}{r^2} \sum_{\alpha, \beta} t_\alpha T_\beta \rightarrow T_\gamma + t_\alpha S_\beta \rightarrow T_\gamma + s_\alpha T_\beta \rightarrow T_\gamma + s_\alpha S_\beta \rightarrow T_\gamma. \quad (13)$$

The notation $t_\alpha S_\beta \rightarrow S_\gamma$ represents a velocity mode α operating on magnetic mode β to produce a third magnetic mode γ . These mode interactions can be computed as various integrals over spherical harmonics, and are shown below:

$$s_\alpha S_\beta \rightarrow S_\gamma = -\frac{K_{\alpha\beta\gamma}}{N_\gamma} \left\{ \nu_\alpha \mu_\alpha s_\alpha \frac{\partial S_\beta}{\partial r} - \nu_\beta \mu_\beta \frac{\partial s_\alpha}{\partial r} S_\beta \right\}, \quad (14)$$

$$t_\alpha S_\beta \rightarrow S_\gamma = -\frac{L_{\alpha\beta\gamma}}{N_\gamma} \nu_\beta t_\alpha S_\beta, \quad (15)$$

$$s_\alpha T_\beta \rightarrow S_\gamma = -\frac{L_{\alpha\beta\gamma}}{N_\gamma} \nu_\alpha s_\alpha T_\beta, \quad (16)$$

$$s_\alpha S_\beta \rightarrow T_\gamma = \frac{L_{\alpha\beta\gamma}}{N_\gamma} \left\{ \nu_\alpha s_\alpha \frac{\partial^2 S_\beta}{\partial r^2} + \left(-\mu_\gamma \frac{\partial s_\alpha}{\partial r} - \nu_\alpha \frac{s_\alpha}{r} \right) 2 \frac{\partial S_\beta}{\partial r} + \nu_\beta \left(\frac{\partial^2 s_\alpha}{\partial r^2} - \frac{2}{r} \frac{\partial s_\alpha}{\partial r} \right) S_\beta \right\}, \quad (17)$$

$$t_\alpha S_\beta \rightarrow T_\gamma = \frac{K_{\alpha\beta\gamma}}{N_\gamma} \left\{ [\nu_\beta \mu_\beta + \nu_\gamma \mu_\gamma] t_\alpha \frac{\partial S_\beta}{\partial r} + \nu_\beta \mu_\beta \left(\frac{\partial t_\alpha}{\partial r} - \frac{2t_\alpha}{r} \right) S_\beta \right\}, \quad (18)$$

$$s_\alpha T_\beta \rightarrow T_\gamma = -\frac{K_{\alpha\beta\gamma}}{N_\gamma} \left\{ \nu_\alpha \mu_\alpha s_\alpha \frac{\partial T_\beta}{\partial r} + \left[\nu_\alpha \mu_\alpha \left(\frac{\partial s_\alpha}{\partial r} - \frac{2s_\alpha}{r} \right) + \nu_\gamma \mu_\gamma \frac{\partial s_\alpha}{\partial r} \right] T_\beta \right\}, \quad (19)$$

$$t_\alpha T_\beta \rightarrow T_\gamma = -\frac{L_{\alpha\beta\gamma}}{N_\gamma} \nu_\gamma t_\alpha T_\beta, \quad (20)$$

$$t_\alpha T_\beta \rightarrow S_\gamma = 0. \quad (21)$$

where $\nu_\alpha = \ell_\alpha(\ell_\alpha + 1)$, $\mu_\alpha = 1/2(\nu_\alpha - \nu_\beta - \nu_\gamma)$, and $N_\gamma = 4\pi\nu_\gamma/2\ell_\gamma + 1$. $K_{\alpha\beta\gamma}$ and $L_{\alpha\beta\gamma}$ are products of the surface harmonics and are called the Adams-Gaunt and Elsasser integrals respectively,

$$K_{\alpha\beta\gamma} = \int_0^{2\pi} \int_0^\pi Y_\alpha Y_\beta Y_\gamma d\Omega,$$

$$L_{\alpha\beta\gamma} = \int_0^{2\pi} \int_0^\pi Y_\alpha \left(\frac{\partial Y_\beta}{\partial \theta} \frac{\partial Y_\gamma}{\partial \phi} - \frac{\partial Y_\gamma}{\partial \theta} \frac{\partial Y_\beta}{\partial \phi} \right) d\Omega.$$

The equations (14)–(21) is solved numerically by using discrete radial profiles and finite differences for estimating the radial derivatives. The equations can be written as an eigenvalue equation of the form:

$$\mathbf{A}\mathbf{b} = \lambda\mathbf{b} \quad (22)$$

where \mathbf{A} is a banded diagonal matrix containing the advection and diffusion terms, \mathbf{b} is the magnetic eigenvector, and λ is its corresponding eigenvalue. This system is solved for the eigenvalue with the largest real component using the ARPACK++ library with the Implicit Restarted Arnoldi Method (IRAM).

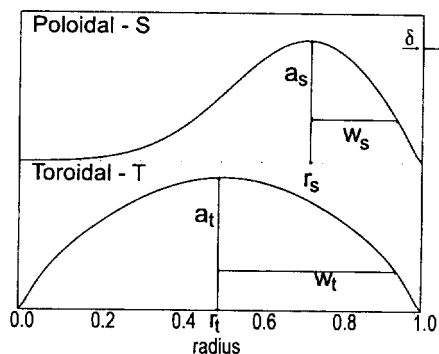


Fig. 2. Parameterization of flows for optimization.

1.2. *Optimized solutions.* Three spherical axisymmetric flow topologies are well-suited for experimental dynamos [9, 10]. Each is described by two profile functions: $\mathbf{t1s1}$ [$s_1^0(r), t_1^0(r)$], $\mathbf{t1s2}$ [$s_2^0(r), t_1^0(r)$], and $\mathbf{t2s2}$ [$s_2^0(r), t_2^0(r)$]. The original study [10] uses profiles which satisfy a mixed set of boundary conditions, namely $s_\ell^m(0) = s_\ell^m(1) = 0$ from non-singularity at the origin and zero outflow at the surface of the sphere, and $t_\ell^m(0) = t_\ell^m(1) = 0$ from non-singularity at the origin and no-slip conditions at the wall. The functions are trigonometric functions which satisfy non-singularity conditions at the origin and no-outflow on the surface of the sphere but do not satisfy no-slip conditions at the outer wall.

We have generalized these radial profile functions to more sophisticated forms suitable for parametric searches:

$$s(r) = a_s r^2 \exp \left\{ -\frac{\delta}{1-r} - \frac{\delta}{r} - \frac{(r-r_s)^2}{w_s^2} \right\}, \quad (23)$$

$$t(r) = a_t r^2 \exp \left\{ -\frac{\delta}{1-r} - \frac{\delta}{r} - \frac{(r-r_t)^2}{w_t^2} \right\}. \quad (24)$$

These flow fields are parametrized by the mode numbers of the imposed flow, the relative amplitude of the toroidal and poloidal flow through a_t and a_s , the position of the poloidal null r_s , the position of peak toroidal rotation r_t , the shear w_t, w_s , and the boundary layer width δ , Fig. 2. The magnitude of the velocity field generated by a particular ratio a_s/a_t is normalized to a peak speed of unity. The optimizations are performed by specifying the topology (choice of ℓ and m functions for the velocity field), solving the eigenvalue problem, and then searching for combinations of parameters which maximize the growth rate at a given Rm . A simple search algorithm [14] is used to find the optimized solutions. Configurations are found with performance up to 50% better than the Dudley and James flows [10]. A lower Rm_c is found for all three configurations, as shown in Table 1.

Table 1. Critical magnetic Reynolds numbers for the Dudley and James flows and also for the optimized flows.

case	Rm_c	Rm_c	Amp	Shift	Width	Edge
	D&J	Optimized				
$\mathbf{t1s1}$	150	72	1:0.12	0.207:0.2	0.256:0.311	0.03
$\mathbf{t1s2}$	95	67	1:0.07	0.36:0.31	0.31:0.385	0.054
$\mathbf{t2s2}$	55	47	1:0.14	0.5:0.46	0.32:0.32	0.05

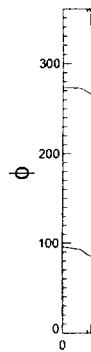


Fig. 3. Profile function of the radial velocity field is seen through the flow along the equator at the equator. The flow enters the

1.3. is an axisymmetric flow the lower excitation flow (see flow conditions at the equator.

The Fig. 3. of the equator mode. The particular dipole mode that the axisymmetric

The understood there must be of a secondary evolution into the approximated flow. At later central field are seen in the figure leads to direction

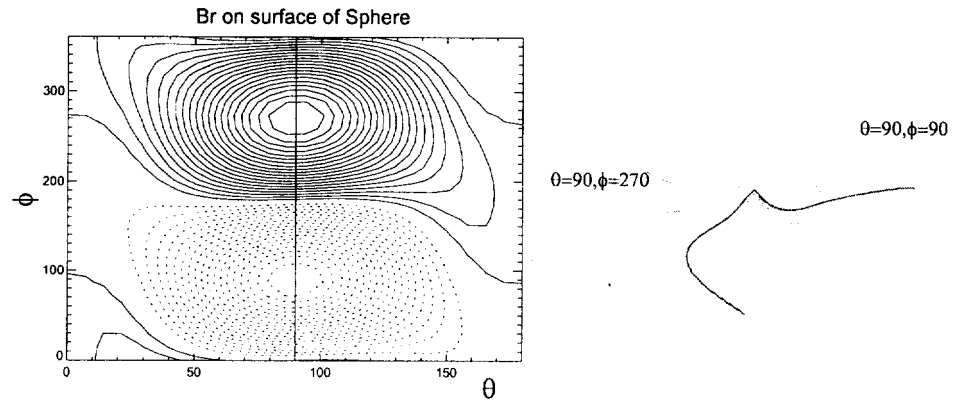


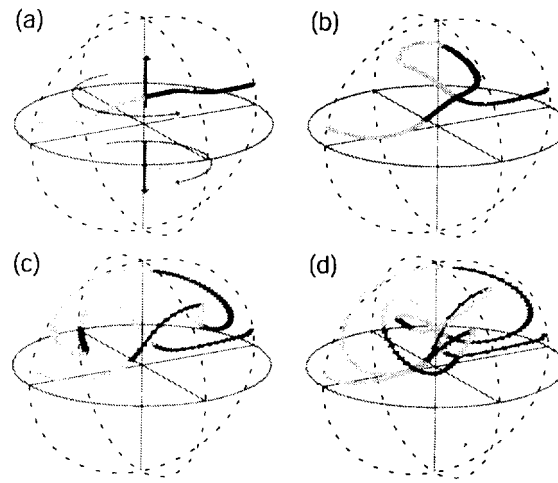
Fig. 3. The magnetic eigenmode of the $t2s2$ dynamo. The left panel is a contour plot of the radial component of the magnetic field on the surface of the sphere. From here it is seen that the magnetic field peaks at the equator. The axis of symmetry for the flows lies along the z -axis. The vacuum field is almost entirely a dipole moment pointing out at the equator. The right panel shows some magnetic field lines for the eigenmode which enter the sphere along the dipole moment.

1.3. *The $t2s2$ Dynamo.* The optimization studies show that the $t2s2$ flow is an attractive candidate for producing a dynamo in the laboratory since it has the lowest Rm_c and thus requires the least sodium and power for producing self-excitation. Furthermore, as shown in the next section, impellers can produce the flow (see Fig. 6 for an example of a $t2s2$ flow produced in the laboratory). The flow consists of two counter-flowing vortices, one above and the other below the equator. These vortices flow out along the poles of the axis of symmetry, flow in at the equator, and have toroidal rotation in opposite directions.

The magnetic eigenmode found from analysis of the $t2s2$ flow is shown in Fig. 3. The magnetic field is predominantly a dipole with its axis in the plane of the equator: the poloidal mode with the largest magnetic energy is the S_2^1 mode. There are, in addition, strong non-dipole components in the core region. In particular, a toroidal component is seen which is in the plane perpendicular to the dipole moment. It should be noted that the eigenvalue is purely real, indicating that the dynamo is purely growing and non-oscillatory. The magnetic field is not axisymmetric and so the dynamo is consistent with Cowling's Theorem.

The mechanism for feedback and self-generation of the magnetic field can be understood most easily by the stretch-twist-fold process. For a dynamo to exist there must be a mechanism for amplification, or stretching, of field lines and there must be a mechanism for positive feedback to occur. Fig. 4 shows the evolution of a seed magnetic field line being distorted by the flows. Here the magnetic field evolution is determined in the limit of infinite Rm where the field lines are frozen into the moving fluid. The first panel shows a magnetic field line corresponding approximately to a dipole seed field perpendicular to the axis of symmetry of the flow. A Lagrangian integration is used to determine the location of the field line at later times as shown in panels (b)-(d). The upwelling of the vortex in the central region stretches the field line upward, while toroidal rotation twists the field around. The field is stretched and reinforces the original magnetic field as seen in panel (d). The stretching (amplification) of the magnetic field is depicted in the figure by the increasing separation of nearby points. In reality, finite resistivity leads to reconnection of field lines in the central region where field lines in opposite directions annihilate each other.

Fig. 4. The time evolution of a magnetic field line being distorted by a $t2s2$ flow. The $t2s2$ flow consists of flows out at the poles (the flow axis of symmetry is vertical) and counter rotating toroidal flows above and below the mid-plane.



Results from the flow optimization studies show that growth rates are sensitive to the ratio of toroidal to poloidal flow. This observation can now be understood geometrically as a requirement that after one twisting, the large loop must come back to the same azimuthal angle as the original dipole field. If the toroidal rotation is too strong or too weak, the stretched magnetic field generates a field at some other toroidal angle and the feedback is insufficient to produce self-excitation.

2. Water experiments. The optimized profiles found above serve as target velocity fields. There is no guarantee, however, that these flows can be easily made in the laboratory. The problem is twofold. First, the inverse problem of finding an impeller that can drive these flows is not easily solved in an experiment. Second, the flows described above are laminar, stationary flows. In reality, flows with $Rm = 100$ have a fluid Reynolds number of 10^7 and are strongly turbulent. At the University of Wisconsin-Madison, flows are studied in a water prototype experiment (shown in Fig. 5) dimensionally identical to a liquid sodium experiment. Liquid sodium and water have nearly identical viscosities and mass densities and thus the water experiment is hydrodynamically identical to an equivalent sodium

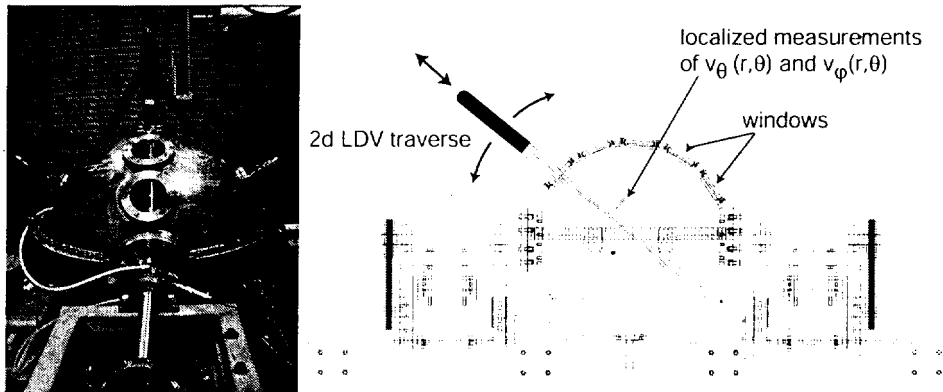


Fig. 5. Schematic of water version of the dynamo experiment. The vessel is a 670 kPa pressure vessel, with two 38 kW motors driving counter rotating impellers. A Laser Doppler Velocimeter (LDV) contains all of the coupling optics to make measurements in the θ and ϕ directions, and is moved by a traverse that allows measurements on an (r, θ) grid.

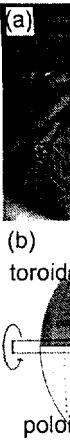


Fig. 6. rotation $V_{\theta, \phi}$ (d values. numer optim

experi is neg water measu experi termin code d

T spheri pressu cavitat the ve Velocit stage Flow 50 kW capab midpl

T helicit direct shafts Impel and a Kört veloci

²So is 1.0).

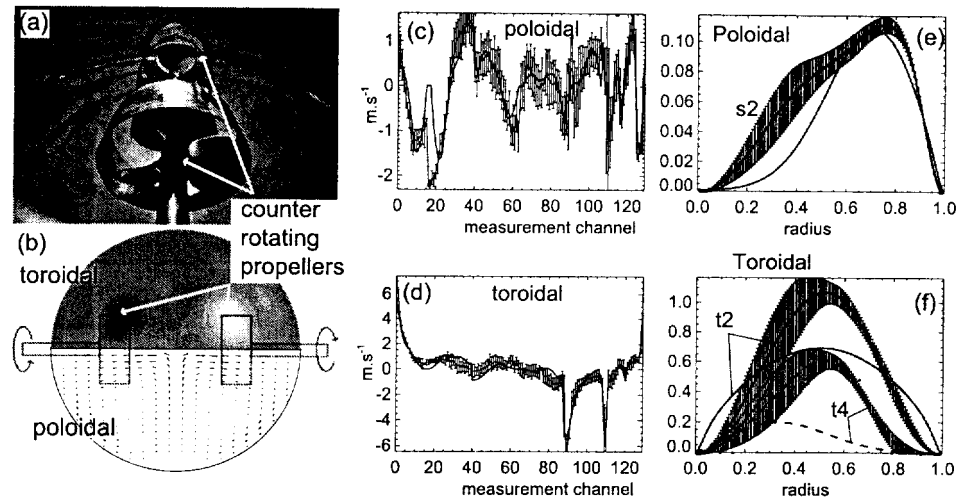


Fig. 6. (a) Photograph of Kört nozzle impellers inside sphere. (b) Contours of toroidal rotation and vector plot of poloidal flows measured in experiment. (c) LDV measured $\bar{V}_{\theta,i}$ (d) LDV measured $\bar{V}_{\phi,i}$. Uncertainties are just statistical spread in the measured values. (e) Fitted profile of $s_2(r)$ (with uncertainty bands) and optimum profile from numerical analysis. (f) Fitted profiles for $t_2(r)$ and $t_4(r)$ (with uncertainty bands and optimum profiles). These measurements correspond to $P_{mech} \approx 20$ kW.

experiment. So long as the magnetic field is small, the Lorentz force on the flow is negligible and flows in the sodium experiment should correspond to flows in the water experiment². The procedure used to evaluate each impeller design involves measuring the mean velocity field produced by a particular impeller in the water experiment, fitting the measurements to a set of $s_i^m(r)$ and $t_i^m(r)$ profiles, and determining the growth rate for the fastest growing eigenmode using the eigenvalue code described above.

The vessel used in the water experiment is a 1 m diameter stainless steel spherical shell with five viewing windows. The windows are designed to withstand pressures up to 670 kPa allowing additional pressure to be applied to prevent cavitation at higher flow speeds. The windows provide a full r and θ scan of the vessel. Flows generated in the experiment are measured using Laser Doppler Velocimetry (LDV). A computer controlled traverse, consisting of a radial scanning stage coupled to a rotating armature positions the LDV optics as shown in Fig. 5. Flows with $\tau 1s1$ and $\tau 2s2$ configurations are generated using the two independent 50 kW motors. The motors are coupled via belt drives to two stainless steel shafts capable of rotation rates up to 1750 RPM. The shafts enter the machine on the midplane through mechanical cartridge seals.

The design adopted for the $\tau 2s2$ experiments uses two impellers of identical helicity with Kört nozzles as shown in Fig. 6. The impellers spin in opposite directions and both produce thrust inward along the poles defined by the impeller shafts. The Kört nozzles are cylindrical rings welded to standard mixing impellers. Impellers without Kört nozzles produce a strong radial jet off the impeller tips and are more effective in producing a s_3^0 velocity field than the desired s_2^0 . The Kört nozzles eliminate this component and lead to smooth s_2^0 profiles. The toroidal velocity is generated in the direction of the impeller rotation.

²Sodium is a solid at room temperature, melts at 98°C, has a specific gravity of 0.97 (water is 1.0), and viscosity of 0.68 cP at 100°C (identical to water at 60°C).

The flows are highly turbulent. The ratio $Re/Rm = 10^5$ for sodium and so the hydrodynamic Reynolds number is of order 10^7 . The Fig. 7 shows the time history for one measurement location of the toroidal velocity. There is a full frequency spectrum for the velocity fluctuations. Not only are there high frequency fluctuations, but there are fluctuations on the resistive time scale of the ($\tau_r \approx 3$ s), as shown in Fig. 7. We have defined the mean velocity (indicated by \bar{V}) to be the average over many resistive times.

2.1. Streamline fitting. The spectral decomposition described above in Eqs (9)–(11) allows a velocity field to be completely described by a set of scalar profiles for t_ℓ^m and s_ℓ^m . Assuming for now that we are only concerned with the axisymmetric component of the velocity field, we can exclude all terms with $m \neq 0$ such that

$$\bar{V}_r(r, \theta) = \sum_{\ell=1}^N \bar{s}_\ell \frac{\ell(\ell+1)}{r^2} P_\ell, \quad \bar{V}_\theta(r, \theta) = \sum_{\ell=1}^N \frac{1}{r} \frac{d\bar{s}_\ell}{dr} \frac{\partial P_\ell}{\partial \theta}, \quad \bar{V}_\phi(r, \theta) = \sum_{\ell=1}^N -\frac{\bar{t}_\ell}{r} \frac{\partial P_\ell}{\partial \theta}. \quad (25)$$

Rather than using spherical harmonics, only the Legendre polynomials $P_\ell(\cos\theta)$ are needed.

The measurements are made at a set of discrete points $r_i, \theta_i, i = 1, M$ where M is the number of measurements made. This set of data can be inverted to find the scalar profiles $s(r)$ and $t(r)$ which best fit the data. Functional forms are chosen for $s(r)$ and $t(r)$ which satisfy the boundary conditions $s(0) = s(1) = t(0) = t(1) = 0$ (such as the optimized radial profiles $\mathbf{a} = [a_\ell, w_\ell, r_\ell]$ from Section 1.2). A cubic spline interpolation is used in this analysis. A non-linear reduced χ^2 minimization is used to find profiles that best fit the data. Since the toroidal and poloidal basis functions are orthogonal, the fits can be performed separately:

$$\chi_s^2(\mathbf{a}) = \sum_{i=1}^{M_\theta} \frac{\left(V_{\theta_i} - \sum_{\ell} \frac{1}{r} \frac{ds_\ell}{dr} \Big|_{\mathbf{a}_\ell} \frac{dP_\ell}{d\theta} \right)^2}{\sigma_{\theta_i}^2}, \quad \chi_t^2(\mathbf{b}) = \sum_{i=1}^{M_\phi} \frac{\left(V_{\phi_i} - \sum_{\ell} \frac{t_\ell(\mathbf{b}_\ell)}{r} \frac{dP_\ell}{d\theta} \right)^2}{\sigma_{\phi_i}^2},$$

where the radial profiles for each spectral mode ℓ are parameterized by the vectors \mathbf{a}_ℓ and \mathbf{b}_ℓ . The V_{θ, ϕ_i} and σ_{θ, ϕ_i} represent the measured velocity and its uncertainty due to fluctuations. The minimization procedure used is a Levenberg–Marquart technique which searches the n -dimensional parameter space defined by the number of elements in \mathbf{a} until χ^2 has been minimized. A typical best fit is shown in Fig. 6. Most flows can be described remarkably well by 4–6 modes and a total of about 20 parameters. The tolerance on the fit itself is large since the flows are quite turbulent. The resulting radial profiles are the mean flow patterns averaged over many eddy turnover times. These profiles are used as input in the eigenvalue code in order to determine the Rm_c of the flow.

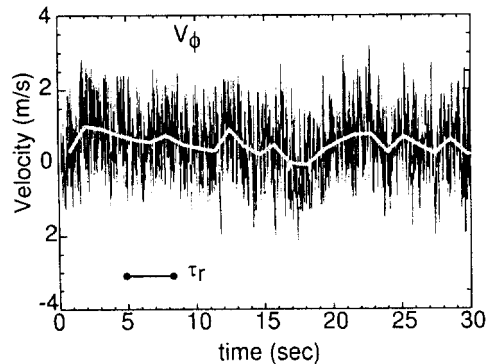


Fig. 7. Time history of $V_{\phi, i}$ measured by LDV. The smooth curve is a running average with a time window equal to the resistive time scale of a similar sodium experiment.

odium and shows the re is a full frequency $\tau_r \approx 3$ s), to be the

above in of scalar with the with $m \neq 0$

$$\frac{\partial P_\ell}{\partial \theta} \quad (25)$$

$$P_\ell(\cos \theta)$$

where M to find the chosen for $t(1) = 0$ A cubic minimization dal basis

$$\left(\frac{\partial P_\ell}{\partial \theta} \right)^2$$

ve vectors certainty Marquart the num-shown in a total of flows are averaged eigenvalue

y of $V_{\phi,i}$ e smooth rage with to the re-a similar

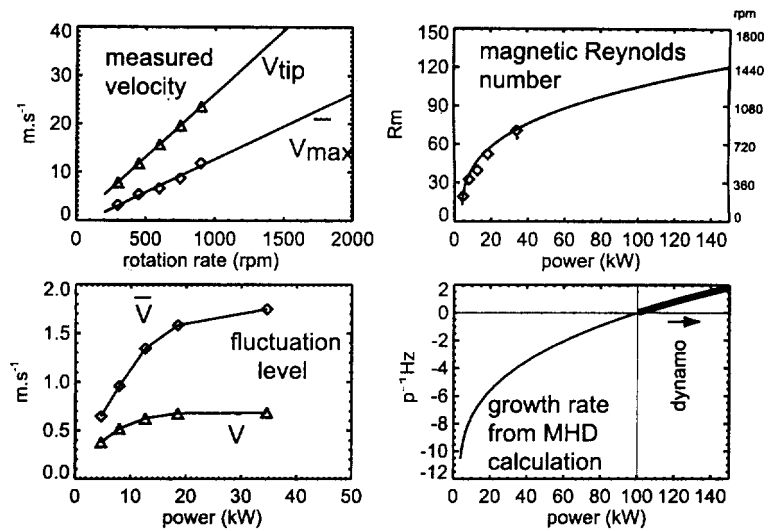


Fig. 8. Numerical extrapolation to full power in the sodium experiment determined from power scan. The growth/damping rate is predicted from the MHD eigenmode code using measured profiles. Positive growth corresponds to dynamo action.

2.2. Extrapolation to sodium experiment. Extrapolating results from the water experiment to the sodium experiment requires several assumptions. First, we assume that the flows will be identical in the sodium experiment. The water experiments are performed over a temperature range 40°C to 60°C, to approximately match the kinematic viscosities (and therefore Re) of sodium at 120°C. Using the measured velocity fields, we then compute the growth rate using the eigenmode code described above. We assume that the flows can be extrapolated to higher Rm than is presently accessible in the water experiment which means we assume the mean velocity field will be unchanged in shape as power is increased. The mechanical input power in the water experiment is currently limited to 30 kW, although in the future this will be increased to 75 kW. An additional limitation is that cooling of the water experiment is limited to 20 kW. Consequently, temperature excursions become large at higher powers. Finally, we have ignored turbulence effects and assumed the measured mean quantities are sufficient for this extrapolation.

The growth rates for the least damped magnetic eigenmode for the flow profiles from Fig. 6 are extrapolated to higher power and are shown in Fig. 8. Flows corresponding to $Rm \approx 70$ are measured which, when scaled to $Rm = 100$, give positive growth rates and are therefore predicted to be dynamos. Note that the definition of Rm for these experiments is based upon the peak of the mean velocity field, not the speed of the impeller tip, or velocity excursions about the mean. Defining Rm based upon the impeller tip would give approximately 3 times the Rm used here (as seen in Fig. 8), but would not be appropriate definition for comparing with the eigenmode calculations.

Perhaps the most troubling assumption is the neglect of turbulence. It may be that the assumption of a static mean flow profile is not applicable. The growth rates of the eigenmodes are sensitive to the details of the flow profiles, and so positive growth may only be observed a fraction of the time. It is also possible that short time-scale (possibly small spatial-scale) fluctuations will affect the growth rate by contributing to an enhanced resistivity such as that produced by a β -effect.

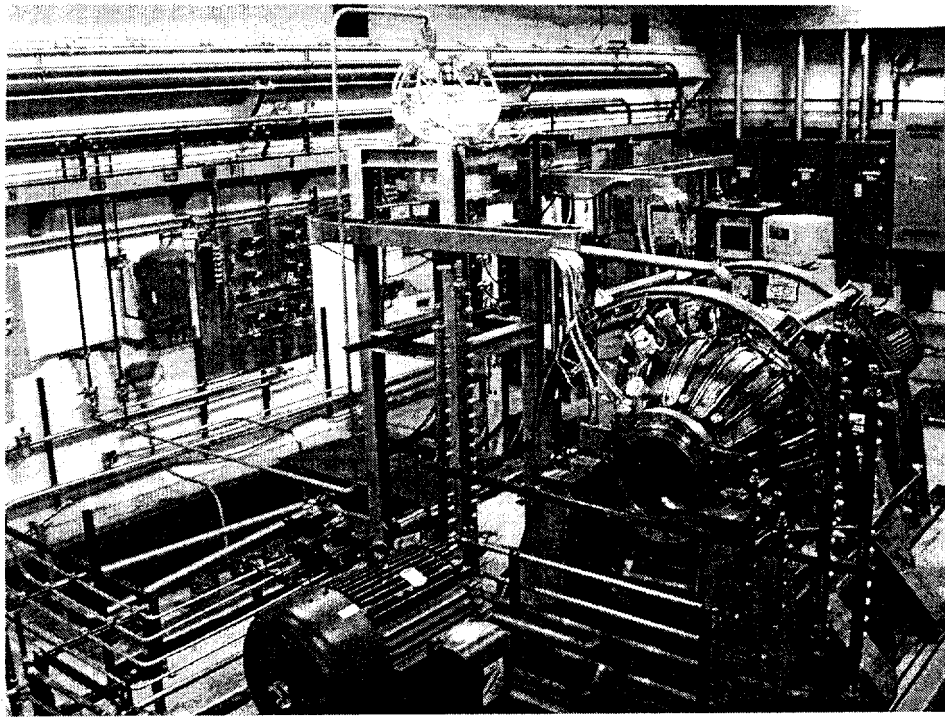


Fig. 9. The Madison Dynamo experiment. This facility handles 300 gallons of liquid sodium and more than 150 kW of mechanical energy for driving flows of order of 10 m/s in a 1 m diameter sphere filled with liquid sodium.


3. Description of the dynamo experiment. The water experiment and the numerical modeling provide confidence that a spherical sodium experiment with a radius of $a = 0.5$ m, approximately 150 kW of power, and peak mean speeds of ≈ 20 m/s is capable of producing a growing magnetic eigenmode. Sodium has $Rm = 4\pi a[m]V[m/s]$, hence an experiment of this scale should be capable of achieving $Rm \geq 100$. The Madison Dynamo Experiment, in its final stages of construction, is shown in Fig. 9.

At the heart of the experiment is a spherical pressure vessel constructed by Ability Engineering rated for pressures up to 700 kPa with two large (40.6 cm diameter) ports for insertion of the impeller assembly. The vessel is constructed of 1.6 cm thick 304L stainless steel. The shell penetration time for the stainless steel is less than 1 ms, compared to the 3 s resistive time for the sodium. The two flanges use spiral-wound Flexitallic gaskets. In addition, eight 5 cm Grayloc ports are placed around the sphere for insertion of probes, and for attaching transfer pipes to the sodium holding tank and the expansion tank.

Two 75 kW three-phase motors drive the impellers and are speed controlled by independent variable frequency drives.

Dynamic imbalance, cavitation and back-reaction are forces that can drive mechanical vibrations in the system. These vibrations are addressed in a number of ways. First, the sphere and motors are firmly mounted on an isolated 50 ton concrete foundation and the impellers and drive shafts are dynamically balanced prior to assembly. The vessel is pressurized with an inert gas to reduce the vibration due to cavitation.

T
 seal fa
 for the
 vessel
 temper
 T
 steel
 the sp
 expans
 resist
 holdin
 by a m
 power
 and c
 oil is
 to ter
 sodiu
 mecha
 remov
 strong
 due to
 T
 coils
 turn,
 coils
 produ
 ment
 the s
 are re
 7
 entire
 level
 the fa
 oxida
 7
 used
 netic
 rately
 the in
 of the
 Foun
 and t
 1. F
 A
 2. A
 F
 3. F
 v



The seals are double mechanical cartridge seals using alpha-silicon carbide seal faces and metallic bellows. Hot oil is used as a buffer, coolant, and lubricant for the seals and is maintained at 240 kPa above the pressure of the experimental vessel. The seals have external heating and cooling circuits to maintain the seal temperature within the specified temperature range of 125–150°C.

The sodium is stored in a 1136 l reservoir placed below ground level in a steel lined vault. Sodium is pneumatically conveyed from the holding tank to the sphere. In addition, there is an expansion tank to accommodate the thermal expansion of the sodium. Two heating techniques are used. First, 60 kW of resistive heating elements are used to heat the bulk of the sodium, in the sphere, holding tank, expansion tank, and transfer lines. The temperature is monitored by a network of thermocouples. Software and hardware feedback loops control the power to the heating elements. The second technique uses an oil based heating and cooling system for controlling the temperature of the sphere. Initially, hot oil is driven through surface-mounted heat exchange tubes to bring the sphere to temperature. While the motors are running, the mechanical heating of the sodium due to viscous dissipation of the flows gives sufficient heating (equal to the mechanical input power). This represents up to 150 kW of heat which must be removed to keep the experiment at constant temperature. The conductivity is a strongly decreasing function of temperature, dropping by roughly a factor of two due to a temperature increase of 100°C. Presently, 35 kW of cooling are available.

The diagnostics and magnetic field subsystems include axial magnetic field coils which can presently apply a 120 G field along the axis of rotation. Two 20 turn, 165 cm diameter coils are mounted coaxially with the experiment. These coils will be used for magnetizing the sodium via a strong toroidal magnetic field produced by differential rotation (the so called ω -effect) and for turn-off experiments. An array of 64 Hall probes (Analog Devices chip AD22151) are located on the surface of the sphere and measure the poloidal field. Magnetic mode numbers are resolved up to $\ell = 4$ and $m = 4$.

The facility is designed to be operated remotely from a control room. The entire experimental area is monitored with arrays of leak detectors, thermocouples, level indicators and hydrogen detectors. A 4000 CFM scrubber system isolates the facility from the outside environment by dissolving any products of sodium oxidation in a water loop.

The sodium experiment will test the validity of the kinematic dynamo model used in numerical modeling of the water experiment. Measurements of the magnetic field will be used to learn whether the stretch-twist-fold mechanism accurately describes the τ_2s_2 dynamo. The experiment will also allow us to establish the importance of effects such as turbulence and back-reaction in a realistic model of the dynamo.

Acknowledgements. This work is supported by the US National Science Foundation, the David and Lucille Packard Foundation, the Research Corporation and the Alfred P. Sloan Foundation.

REFERENCES

1. P. ROBERTS, T. JENSEN. Homogeneous dynamos: theory and practice. *Phys. Fluids B*, vol. 5 (1993), pp. 2657–2662.
2. A. HERZENBERG. Geomagnetic dynamos. *Phil. Trans. Roy. Soc. A*, vol. 250 (1958), pp. 543–583.
3. F. LOWES, I. WILKINSON. Geomagnetic dynamo: a laboratory model. *Nature*, vol. 198 (1963), pp. 1158–1160.

4. F. LOWES, I. WILKINSON. Geomagnetic dynamo: an improved laboratory model. *Nature*, vol. 219 (1968), pp. 717-718.
5. R. STIEGLITZ, U. MÜLLER. Experimental demonstration of a homogeneous two-scale dynamo. *Phys. Fluids*, vol. 13 (2001), pp. 561-564.
6. A. GAILITIS, O. LIELAUSIS, S. DEMENT'EV, E. PLATACIS, A. CIFERSONS, G. GERBETH, TH. GUNDRUM, F. STEFANI, M. CHRISTEN, H. HÄNEL, G. WILL. Detection of a flow induced magnetic field eigenmode in the Riga dynamo facility. *Phys. Rev. Lett.*, vol. 84 (2000), pp. 4365-4368.
7. P. ODIER, J. PINTON, S. FAUVE. Advection of a magnetic field by a turbulent swirling flow. *Phys. Rev. E*, vol. 58 (1998), p. 7397.
8. N. PEFFLEY, A. CAWTHORNE, D. LATHROP. Toward a self-generating magnetic dynamo: The role of turbulence. *Phys. Rev. E*, vol. 61 (2000), pp. 5287-94.
9. D. GUBBINS. Numerical solutions of the kinetic dynamo problem. *Phil. Trans. R. Soc. Lond. A*, vol. 274 (1973), pp. 493-521.
10. M. DUDLEY, R. JAMES. Time-dependent kinematic dynamos with stationary flows. *Proc. R. Soc. Lond. A*, vol. 425 (1989), p. 407.
11. R. HOLME, J. BLOXHAM. The magnetic fields of Uranus and Neptune: methods and models. *J. Geophys. Res.*, vol. 101 (1996), p. 2177.
12. R. HOLME. Three-dimensional kinematic dynamos with equatorial symmetry: application to the magnetic fields of Uranus and Neptune. *Phys. of the Earth And Planetary Int.*, vol. 102 (1997), pp. 105-22.
13. E. BULLARD, H. GELLMAN. Homogeneous dynamos and terrestrial magnetism. *Phil. Trans. R. Soc. Lond. A*, vol. 247 (1954), pp. 213-278.
14. B. PRESS, W.H. FLANNERY ET AL. *Numerical Recipes in C*. (1988), p. 329.

Received 7.09.2001

We d
and ro
experi
etry, a
mecha

I
lieved
planet
large
and E
requir
search
turbu
tions
In ou
namic
streng
affect

V
labor
dicat
attem
motiv
at Ka
I
force
Sec. 3
Final
sodium

I
action
spher
1.5 c
coaxi
with
pulse
for o
magn
rate i
the s